

X-Ray Wind Tomography of the highly absorbed HMXB IGR J17252 – 3616[★]

A. Manousakis^{1,2} and R. Walter^{1,2}

¹ ISDC Data Center for Astrophysics, Chemin d’Ecogia 16, CH-1290 Versoix, Switzerland
e-mail: Antonios.Manousakis@unige.ch

² Observatoire de Genève, Université de Genève, Chemin des Maillettes 51, CH-1290 Versoix, Switzerland

Received XXX; accepted XXX

ABSTRACT

Context. About 10 persistently highly absorbed super-giant High-Mass X-ray Binaries (sgHMXB) have been discovered by INTEGRAL as bright hard X-ray sources lacking bright X-ray counterparts. Besides IGR J16318-4848 that features peculiar characteristics, the other members of this family share many properties with the classical wind-fed sgHMXB systems.

Aims. Our goal is to understand the specificities of highly absorbed sgHMXB and in particular of the companion stellar wind, thought to be responsible for the strong absorption.

Methods. We have monitored IGR J17252 – 3616, a highly absorbed system featuring eclipses, with *XMM-Newton* to study the variability of the column density and of the Fe $K\alpha$ emission line along the orbit and during the eclipses. We also built a 3D model of the structure of the stellar wind to reproduce the observed variability.

Results. We first derived a refined orbital solution for this system built from *INTEGRAL*, *RXTE* and *XMM-Newton* data. The *XMM-Newton* monitoring campaign revealed significant variation of intrinsic absorbing column density along the orbit and of the Fe $K\alpha$ line equivalent width around the eclipses. The origin of the soft X-ray absorption is modeled with an dense and extended hydrodynamical tail, trailing the neutron star. This structure extends along most of the orbit, indicating that the stellar wind is strongly disrupted by the neutron star. The variability of the absorbing column density suggests that the wind velocity is smaller ($v_\infty \approx 400$ km/s) than observed in classical systems. This can also explain the much stronger density perturbation inferred from the observations. Most of the Fe $K\alpha$ emission is generated in the most inner region of the hydrodynamical tail. This region, that extends over a few accretion radii, is ionized and does not contribute to the soft X-ray absorption.

Conclusions. We have built a qualitative model of the stellar wind of IGR J17252 – 3616 that can represent the observations and suggest that highly absorbed systems have a lower wind velocity than classical sgHMXB. This proposal could be tested with detailed numerical simulations and high-resolution infrared/optical observations. If confirmed, it may turn out that half of the persistent sgHMXB have low stellar wind speeds.

Key words. X-Rays:binaries – Stars: pulsars : individuals: IGR J17252 – 3616= EXO 1722-363 –

1. Introduction

High mass X-ray binaries (HMXB) consist of a neutron star or a black-hole fueled by the accretion of the wind of an early type stellar companion. Their X-ray emission, a measure of the accretion rate, shows a variety of transient to persistent patterns. Outbursts are observed on timescales from seconds to months and dynamical ranges varying by factors of 10^4 . The majority of the known HMXB are Be/X-ray binaries (Liu et al. 2006), with Be stellar companions. These systems are transient, featuring bright outburst with typical duration on the order of several weeks (Charles & Coe 2006). A second class of HMXBs harbour OB supergiants companions (sgHMXBs) feeding the compact object through strong, radiatively driven, stellar winds or Roche lobe overflow. Thanks to INTEGRAL, the number known sgHMXB systems tripled during the last decade (Walter et al. 2006).

Highly absorbed sgHMXB were discovered by *INTEGRAL* (Walter et al. 2004) and are characterized by strong and persistent soft X-ray absorption ($N_H > 10^{23}$ cm⁻²). When detected, these systems have short orbital periods and long spin periods (Walter et al. 2006). They corresponds to the category of wind-fed accretors in the Corbet diagram (Corbet 1986).

IGR J17252 – 3616 has been detected by *ISGRI* on board *INTEGRAL* on February 9, 2004 among other hard X-ray sources (Walter et al. 2004, 2006). The source has first been detected by *EXOSAT* (EXO 1722-3616) as a weak soft X-ray source, back in 1984 (Warwick et al. 1988). In 1987, *Ginga* performed a pointed observations and revealed a highly variable X-ray source, X1722-363, with a pulsations of ~ 413.9 sec (Tawara et al. 1989). Further *Ginga* observations revealed the orbital period of 9-10 days and a mass of the companion star of $\sim 15 M_\odot$ (Takeuchi et al. 1990). Both papers concluded that the system was a high mass X-ray binary (HMXB).

INTEGRAL and *XMM* observations of IGR J17252 – 3616 allowed to identify the infrared counterpart of the system and to accurately measure the absorbing column density and refine the spin period of the system. Thanks to the eclipses, an accurate orbital period could be derived from *INTEGRAL* data (Zurita Heras et al. 2006). Further *RXTE* observations re-

Send offprint requests to: A. Manousakis

[★] Based on observations obtained with *XMM-Newton* and *INTEGRAL*, two ESA science mission with instruments, data centers, and contributions directly funded by ESA Member States, NASA, and Russia.

vealed a highly inclined system ($i > 61^\circ$) with a companion star of $M_* \lesssim 20 M_\odot$ and $R_* \sim 20 - 40 R_\odot$ (Thompson et al. 2007). Recent VLT observations provided the companion spectral type (Chaty et al. 2008; Mason et al. 2009a) and radial velocities measurements (Mason et al. 2009b). Its spectral energy distribution can be characterized by a temperature of $T_* \sim 30$ kK and a reddening of $A_V \sim 20$ (Rahoui et al. 2008).

In this paper, we report on a monitoring campaign of IGR J17252 – 3616 performed with *XMM-Newton* along the orbit in order to estimate the structure of the stellar wind and of the absorbing material in the system. We describe the data and their analysis in Section 2, a refined orbital solution in section 3 and present the evolution of the X-ray spectral shape along the orbit in section 4. In section 5, we present and discuss a 3D model of the structure of the stellar wind that can reproduce the observations and conclude in section 6.

2. Data reduction and analysis

2.1. XMM-Newton

Pointed observations of IGR J17252 – 3616 were performed between August and October 2006 with *XMM-Newton* (Jansen et al. 2001). We scheduled 9 observations to cover the orbital phases : 0.01, 0.03, 0.08, 0.15, 0.27, 0.40, 0.65, 0.79, and 0.91. In addition, we used one observation of 2004 with a phase of 0.37. The observations are summarized in table 1.

The Science Analysis Software (XMM-SAS) version 9.0.0¹ was used to produce event lists for the EPIC-pn instrument (Strüder et al. 2001) by running `epchain`. Barycentric correction and good time intervals (GTI) were applied. Photon pile-up and/or out-of-time event were not identified among the data. High level products (i.e., spectra and lightcurves) were produced using `evselect`². Spectra and lightcurves were built by collecting double and single events in the energy range 0.2 - 10 keV. The lightcurves were built using 5 sec time bins. The spectra were re-binned to obtain 25 counts/bin for low count rate observations and 100 counts/bin for high count rate observation.

In one dataset (ObsID 0405640701, ~ 19 ksec), the count rate above 10 keV has a very peculiar behavior, increasing monotonically with time. As this does not affect the background subtracted source lightcurve significantly we kept the entire data for pulse arrival times determination. Standard GTI was used for spectral analysis.

2.2. INTEGRAL

We reanalysed the complete hard X-ray light-curve of IGR J17252 – 3616 obtained with *ISGRI* (Lebrun et al. 2003) on board *INTEGRAL* (Winkler et al. 2003). We extracted the 22–40 keV light-curve using the HEAVENS interface (Walter 2010) provided by the *INTEGRAL* Science Data Centre³ (Courvoisier et al. 2003). The lightcurve includes all public data available on IGR J17252 – 3616 from 2003-01-29 06:00:00 to 2009-04-08 00:28:48 UTC. The effective exposure time on source is ~ 3.6 Msec.

3. Timing analysis and orbit determination

3.1. Orbital Period from INTEGRAL

We have used the Lomb-Scargle (Press & Rybicki 1989) technique to determine the orbital period from the *INTEGRAL* light-curve and obtained $P_{orb} = 9.742 \pm 0.001$ days. Figure 1 shows (upper panel) the Lomb-Scargle power around the orbital period (dashed line). This period was used to refine the orbital solution (section 3.3). The lower panel of figure 1 shows the light-curve folded with the newly derived orbital period. The eclipse is clearly detected with the count rate dropping to zero.

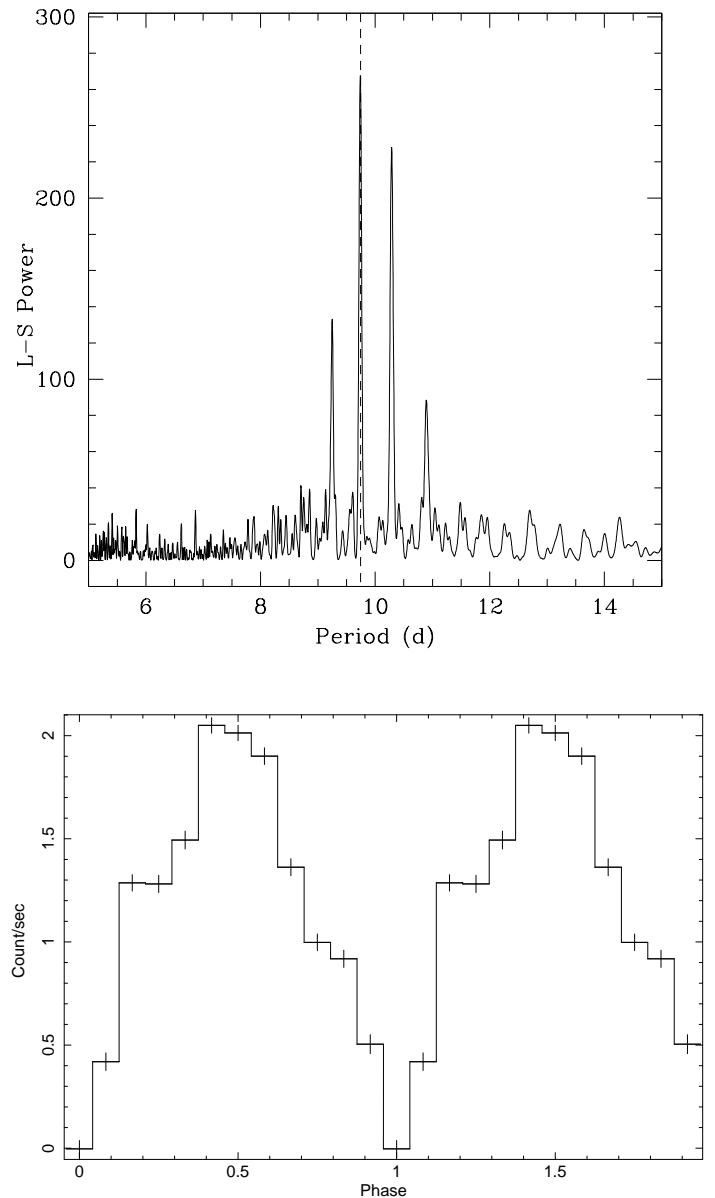


Fig. 1. Top: Lomb-Scargle periodogram obtained from the *INTEGRAL* 22-40 keV lightcurve. Bottom: *INTEGRAL* lightcurve folded with a period of 9.742 days.

¹ <http://xmm.esac.esa.int/sas/>

² <http://xmm.esac.esa.int/sas/current/howtouseas.shtml>

³ <http://www.isdc.unige.ch/heavens>

Table 1. XMM-Newton observation log listing the revolution number, the start time, the effective exposure, the source counts, and the phase, calculated at the middle of each observation using the orbital solution obtained with fixed orbital period (table 3).

ObsID	#	Revolution	Start time (UT)	Effective exposure (ks)	Source counts	Phase (± 0.01)
0405640201	1	1231	2006-08-29T03:02:58	19.2	5.4×10^2	0.03
0405640301	2	1232	2006-08-31T16:37:44	4.1	1.4×10^4	0.27
0405640401	3	1234	2006-09-04T06:35:33	5.6	7.9×10^3	0.65
0405640501	4	1235	2006-09-06T19:33:10	5.4	9.5×10^2	0.91
0405640601	5	1236	2006-09-08T10:03:38	7.9	3.8×10^2	0.08
0405640701	6	1239	2006-09-15T07:23:45	2.8	1.7×10^3	0.79
0405640801	9	1247	2006-10-01T03:24:26	9.4	2.3×10^4	0.40
0405640901	8	1246	2006-09-28T14:36:53	11.3	1.9×10^4	0.15
0405641001	7	1245	2006-09-27T07:27:58	9.4	6.5×10^2	0.01
0206380401	10	785	2004-03-21T13:23:09	8.6	4.7×10^4	0.37

Table 2. Pulse Arrival Times and derived pulse period. Last column gives the Lomb-Scargle periods. We couldn't get a good S/N LS diagram for observation 0405640301.

ObsID	PAT (HJD) (± 0.00011)	Pulse period (s)	L-S period (s)
0405640301	53978.74948	414.3 ± 0.1	-
0405640401	53982.32329	414.0 ± 0.1	417.4 ± 0.6
0405640701	53993.45320	414.2 ± 0.2	414.6 ± 0.1
0405640801	54009.24191	414.2 ± 0.1	414.2 ± 0.4
0405640901	54006.75737	413.8 ± 0.1	413.8 ± 0.3

3.2. Pulse Arrival Times

Pulse arrival times (PATs, hereafter) have been obtained from the broad-band 0.2-10 keV lightcurves obtained by *XMM-Newton*. Close to the eclipse ($\phi = 0.03, 0.08, 0.91, 0.01$), when the compact object is behind the massive star, pulses could not be detected. We did not extract PATs for the observation of 2004.

In order to determine the PATs we used a pulse profile template. This template is derived by folding the lightcurve from observation 0405640801 with a period of 414.2 sec, obtained using the Lomb-Scargle technique (Press & Rybicki 1989). This observation was selected because the source was very bright for a long and almost uninterrupted exposure.

A sequence of pulse profile template was fit to each individual lightcurve. This sequence is characterized by: (i) the time of a pulse at the middle of the observation, (ii) the pulse period, and (iii) the amplitudes of each pulse. This assumes that the pulse period is reasonably constant during each observation.

The statistical errors on the pulse time and period are typically 0.01 sec and 0.1 sec, respectively. Table 2 lists the pulse times and the spin period obtained at the middle of each observation. The spin periods were always consistent with the Lomb-Scargle period of each run.

The PAT accuracy is however limited by the systematic error related to the assumed pulse template. Using a different pulse profile template (derived from observation 0405640901) produces PAT with offset of 8 to 12 sec from the values listed in table 2. We adopted a systematic error of 10 sec.

3.3. Orbital Solution

We have derived the orbital solution using the PATs of the *RXTE* observation obtained by Thompson et al. (2007, Epoch 3), and the PATs derived above from *XMM* data.

The orbital solution is obtained by comparing the observed pulse arrival delays ($t_n - t_0 - nP_0 - \frac{1}{2}n^2P_0\dot{P}$) to the expected ones $\alpha_x \sin i \cos[2\pi(t_n - T_{90})/P_{orb}]$ (Levine et al. 2004). The orbital parameters (the orbital period, P_{orb} ; the projected semi-major axis, $\alpha_x \sin i$; the reference time corresponding to mid-eclipse, T_{90}) are assumed to be constant. To account for pulse evolution, two set of pulse parameters (spin period at time t_0 , P_0 ; spin period derivative, \dot{P}) have been used for the *RXTE* and *XMM* campaigns. The pulse number n is given by the nearest integer to $n = (t_n - t_0)/(P_0 + 0.5\dot{P}(t_n - t_0))$.

We have performed a combined fit for the *RXTE* and *XMM* observations. We derived the orbital solutions by (i) allowing all the parameters to vary freely and (ii) by fixing the orbital period to the value derived from *INTEGRAL* data. The resulting parameters are listed in table 3. We could also obtain an upper limit (90%) of $e < 0.15$ on the eccentricity. The latter has been achieved by adding the first-order term in a Taylor series expansion in the eccentricity (Levine et al. 2004). The *RXTE* and *XMM* orbital solutions are comparable and the resulting parameters are consistent within the errors.

The folded lightcurve obtained by *INTEGRAL* derived orbital period (fig. 1, lower panel) results in a pulse fraction $\sim 100\%$. For the rest of the analysis, we used the orbital solution obtained with fixed P_{orb} (table 3).

Figure 2 shows the resulting pulse arrival times delays (fixed P_{orb}) for both *RXTE* and *XMM* data together with the best-fit orbital solution.

4. Spectral analysis

The spectral analysis was performed using the XSPEC⁴ package version 11.3.2ag (Arnaud 1996). In order to use the χ^2_ν statistics, we grouped the data to have at least 25 (faint spectra) and up to 100 (bright spectra) counts per bin. We initially fitted the observed spectra using a phenomenological model made of an intrinsically absorbed cutoff power law, a blackbody soft excess, and a gaussian Fe $K\alpha$ line (wabs*(bb+gauss+vphabs*cutoff)). The centroid of the iron line is compatible with $E_c \sim 6.40 \pm 0.03$ keV at all epochs.

The spectra are always strongly absorbed below ~ 3 keV and feature an iron K-edge at $\sim 7.2 \pm 0.2$ keV. We first fit each spectrum with all parameters free, excepting the galactic absorption, fixed to $N_H = 1.5 \times 10^{22}$ cm⁻² (Dickey & Lockman 1990).

⁴ <http://xspec.gsfc.nasa.gov>

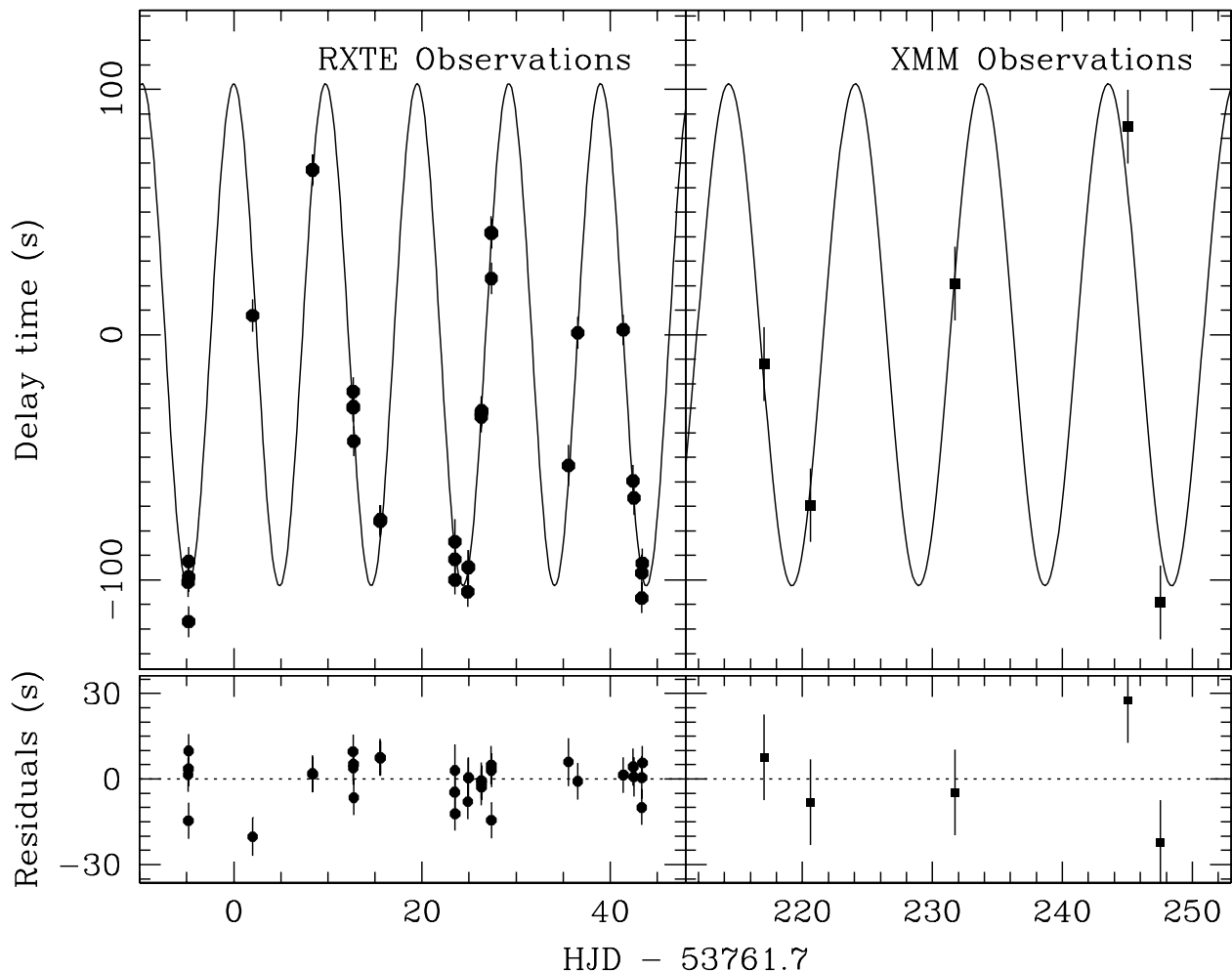


Fig. 2. Delays (top) and residuals (bottom) derived from the fixed P_{orb} orbital solution compared to the data. *Left:* *RXTE* data are taken from Thompson et al. (2007). *Right:* *XMM – Newton* data from this work.

Table 3. Orbital solution for IGR J17252 – 3616. The errors have been calculated at 90% confidence level. The errors on the arrival times t_0 are 0.00001 and 0.0001 days for *RXTE* and *XMM*, respectively. The last column shows the result from Thompson et al. (2007) for comparison.

	Units	Free P_{orb}	Fixed P_{orb}	RXTE Epoch 3
t_0^{XTE}	HJD	53761.73144	53761.73142	53761.73126
P_0^{XTE}	s	413.889 ± 0.004	413.889 ± 0.005	413.894 ± 0.002
\dot{P}^{XTE}	$\mu\text{s s}^{-1}$	-0.010 ± 0.002	-0.010 ± 0.003	-0.0106 ± 0.0001
t_0^{XMM}	HJD	53978.7494	53978.7495	-
P_0^{XMM}	s	413.86 ± 0.04	413.84 ± 0.04	-
\dot{P}^{XMM}	$\mu\text{s s}^{-1}$	0.98 ± 0.04	1.01 ± 0.03	-
$\alpha_x \sin i$	lt-s	102 ± 8	101 ± 2	101 ± 4
P_{orb}	d	9.76 ± 0.02	9.742 (fixed)	9.78 ± 0.04
T_{90}	HJD	53761.62 ± 0.1	53761.69 ± 0.1	53761.60 ± 0.09
χ^2_ν		1.5 (30)	1.65 (31)	1.45 (28)

Some parameters (photon index, cutoff energy, blackbody temperature, absorber Fe metallicity) did not vary (within the 90% errors) among the observations and were fixed to their average values of $E_C = 8.2$ keV, $\Gamma = 0.02$, and $kT_{BB} = 0.5$ keV,

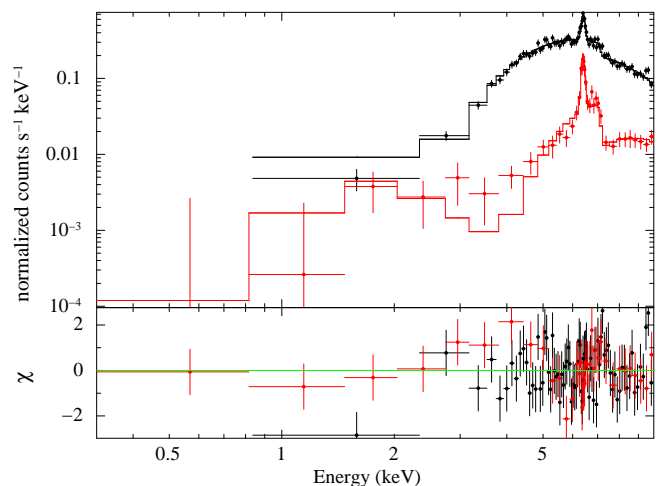


Fig. 3. *Top:* Folded model and data for $\phi=0.65$ (black) and $\phi=0.91$ (red). *Bottom:* The corresponding residuals using the model described in the text with the parameters from table 4.

$Z=1 Z_\odot$. The Fe line energy is fixed to $E=6.4$ keV, with a nar-

row width. Two representative spectra of our observations are displayed in figure 3.

The intrinsic absorbing column density and the normalization of each component could vary freely. The best fit parameters are listed in table 4. Figure 4 shows the variation of all these parameters and of the unabsorbed 2-10 keV flux and Fe $K\alpha$ equivalent width (EW). The unabsorbed Fe $K\alpha$ EW was calculated by setting the intrinsic absorbing column density to zero. All the spectral fits were good resulting in $\chi^2_\nu \approx 0.8 - 1.4$, apart for the $\phi=0.03$ observation providing a poor fit. During the eclipse, some parameters are poorly constrained.

The unabsorbed continuum flux (fig. 4-f) is of the order of $\sim 5 \times 10^{-11}$ erg cm $^{-2}$ s $^{-1}$ outside of the eclipse. Variations are observed between $(2 - 10) \times 10^{-11}$ erg cm $^{-2}$ s $^{-1}$ and they can be interpreted as variation of the accretion rate (\dot{M}). During the eclipse the continuum flux drops by a factor of ~ 200 and remains stable at the level of $F_{unabs}^{2-10keV} \approx (7 \pm 1) \times 10^{-13}$ erg cm $^{-2}$ s $^{-1}$.

The intrinsic absorbing column density (fig. 4-b) is persistently high ($\gtrsim 10^{23}$ cm $^{-2}$). Significant variations are detected for $\phi = 0.2 - 0.4$ and close to the eclipse, reaching values of $N_H \sim 9 \times 10^{23}$ cm $^{-2}$.

The normalization of the blackbody component (fig-4-c) does not show any variability, although the low energy part of the spectrum is poorly constrained. The normalization of the blackbody component is compatible with $\sim 10^{33}$ erg s $^{-1}$ assuming a distance of 8 kpc. The very high intrinsic absorbing column density rules out the neutron star as the origin of the soft excess.

The flux and EW of the Fe $K\alpha$ line are displayed on figure 4-d and 4-e, respectively. Both components show significant variations indicating that the region emitting the line is at least partially obscured by the mass-donor star.

As the X-ray continuum illuminating the gas emitting the Fe fluorescent line cannot be measured during the eclipse we calculated a corrected Fe $K\alpha$ EW by assuming a constant continuum flux of 1.8×10^{-3} ph keV $^{-1}$ cm $^{-2}$ s $^{-1}$ (fig. 7).

5. Discussion

5.1. Constraining the physical parameters of the system.

In the previous sections we have derived an orbital solution (table 3) yielding a mass function $f = 4\pi^2(\alpha_x \sin i)^3 / GP_{orb}^2 = M_{OB} \sin^3 i / (1 + q)^2 \approx 11.7 \pm 0.7 M_\odot$. This is consistent with a high mass x-ray binary system.

Adopting an inclination $i = 90^\circ$ we infer a mass $M_{OB} \sim 14 M_\odot$ for the donor star. Radial velocity observation showed $q = M_X / M_{OB} \sim 0.1$ (Mason et al. 2009b). Using an upper limit on the mass of $\sim 20 M_\odot$ (Thompson et al. 2007) constrain the inclination of the orbit $i > 70^\circ$. Mason et al. (2009b) estimated an inclination $i \approx 75^\circ - 90^\circ$. With this value the mass of the donor star is constrained in the range $M_{OB} \approx 14 - 17 M_\odot$. The mass ratio and the donor mass imply a neutron star mass $M_{NS} = 1.4 - 1.7 M_\odot$. Both the masses of the donor star and of the compact object are roughly similar (within a factor of 2) to Vela X-1 (Quaintrell et al. 2003; van Kerkwijk et al. 1995).

The separation of the system could be derived from the duration of the eclipse and the inclination (Joss & Rappaport 1984). For the eclipse duration of $\Delta\phi \approx 0.18 \pm 0.02$ (i.e. 1.75 days) we can estimate the separation $\alpha_x \approx 1.7 - 1.8 R_*$. The Roche lobe (R_L) of the system scales from $R_L = 0.99 - 1.06 R_*$ assuming a synchronous rotation (Joss & Rappaport 1984). This means that the system is very close to fill its Roche lobe and form an accretion disk, although no significant spin-up has been observed.

Using our VLT observations, Mason et al. (2009a) performed near-IR spectroscopy of IGR J17252 – 3616 and concluded that the donor star is a B0-B5 I to B0-B1 Ia with effective temperature $T_{eff} = 22-28$ kT and a stellar radius of $R_* = 22-36 R_\odot$. Based on a spectroscopic determination, we can translate it into absolute numbers for the separation ($\alpha_x \approx 37 - 64 R_\odot$) and the Roche lobe radius ($R_L \approx 22 - 38 R_\odot$).

The unabsorbed 2-10 keV source flux is in the range $(0.2 - 1.3) \times 10^{-10}$ erg s $^{-1}$ cm $^{-2}$. Adopting a mean value of $(0.8 \pm 0.3) \times 10^{10}$ erg s $^{-1}$ cm $^{-2}$ and assuming a distance of 8 kpc (Mason et al. 2009a) the inferred 2-10 keV unabsorbed luminosity is $L_X \sim 10^{36}$ erg s $^{-1}$. Assuming accretion as the source of energy ($L_X = \epsilon \dot{M} c^2$), we can estimate a mass accretion rate of $\dot{M} \sim 10^{-9} M_\odot$ yr $^{-1}$ similar to that of Vela X-1 (Fürst et al. 2010).

During the eclipse, the X-ray luminosity drops by a factor of ~ 200 resulting a $L_X \sim 5 \times 10^{33}$ erg s $^{-1}$. As OB stars are emitting in X-rays with a luminosity $L_X \sim 10^{31-32}$ erg s $^{-1}$ (Güdel & Nazé 2009), this emission is probably dominated by scattering in the stellar wind (Haberl 1991).

Hickox et al. (2004) have discussed the origin of soft X-ray excesses in many types of accreting pulsars. It is likely, that the fairly constant soft X-ray excess observed in IGR J17252 – 3616 is emitted by recombination lines (Schulz et al. 2002) in a region of the wind larger than the stellar radius (Watanabe et al. 2006).

For a spherically symmetric stellar wind, one would expect to have smooth and predictable variations on the absorbing column density along the orbit. In particular observations on the same line of sight or symmetric when compared to the eclipse must result in different, respectively identical, column densities. Our observing strategy resulted in $N_H(\phi = 0.15) \approx N_H(\phi = 0.37)$, $N_H(\phi = -0.35) > N_H(\phi = 0.37)$ and $N_H(\phi = -0.35) \approx N_H(\phi = -0.21)$, ruling out a spherical geometry.

5.2. Stellar wind structure

We have constructed a 3D model of the OB supergiant stellar wind in order to simulate the variability of the intrinsic column density (N_H) and of the Fe $K\alpha$ line equivalent width (EW), along the orbit, and to compare them with the observations. We have assumed a distance $D \approx 8$ kpc (Mason et al. 2009a), a circular orbit ($e = 0$) and an edge-on geometry ($i = 90^\circ$).

Variability of N_H along the orbit

We first investigate the behavior of the intrinsic column density, N_H , as a function of phase, to reveal the structure of the wind along the orbit. We approximated the wind structure with two components, the unperturbed wind (ρ_{wind}) and a tail-like hydrodynamic perturbation (ρ_{tail}) related to the presence of the neutron star. Tail-like structures are predicted by hydrodynamical simulations (Blondin et al. 1990) but produce N_H , up to $\sim 10^{22}$ cm $^{-2}$, too small to account for the variability observed in IGR J17252–3616.

The unperturbed stellar wind has been modeled by assuming a standard wind profile (Castor et al. 1975),

$$v(r) = v_\infty \left(1 - \frac{R_*}{r}\right)^\beta$$

where $v(r)$ is the wind velocity at distance r from the stellar center, v_∞ is the terminal velocity of the wind, and β is a parameter describing the wind gradient. The conservation of mass provides the radial density distribution of the stellar wind. The unperturbed stellar wind is a good approximation within the orbit

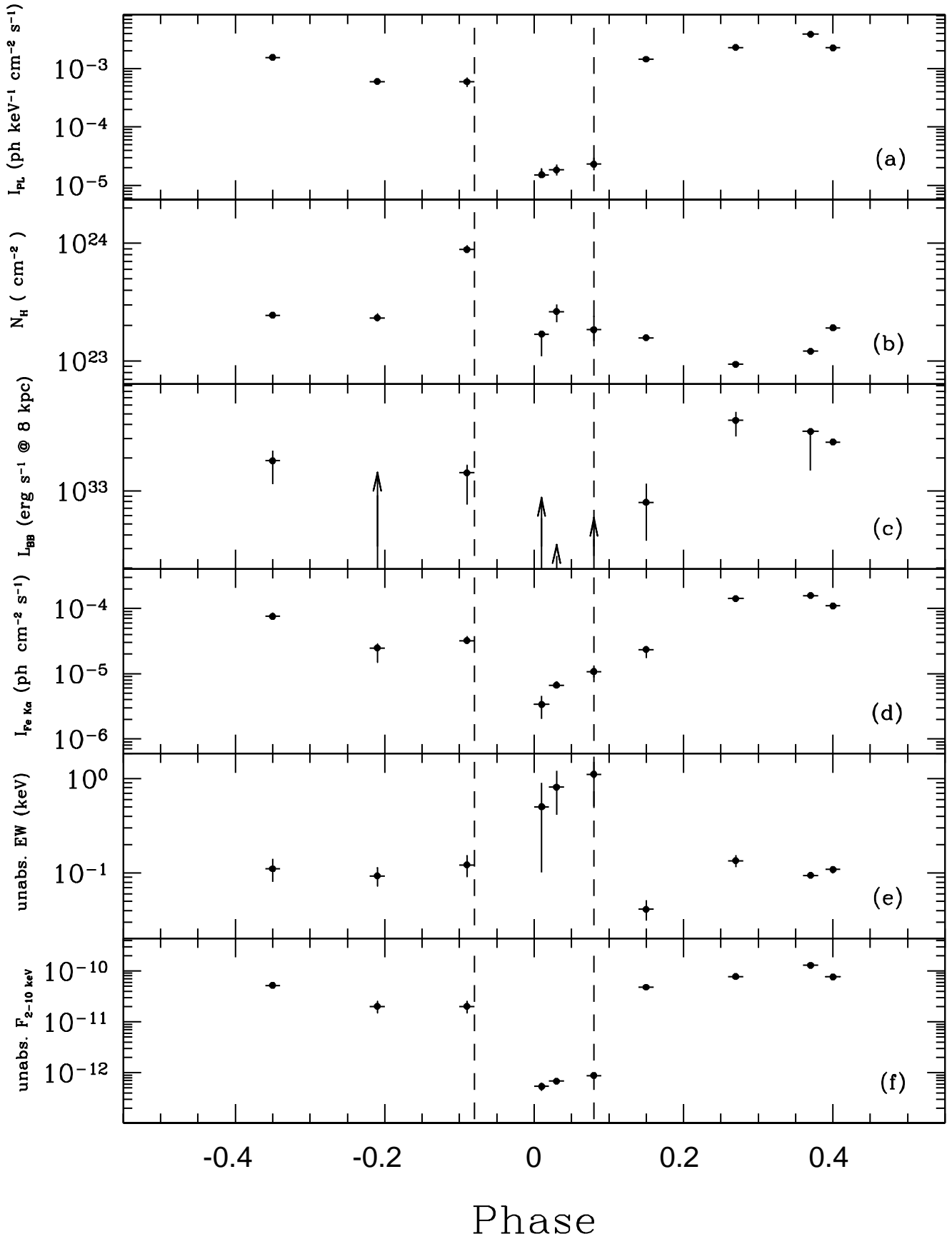


Fig. 4. Spectral variability along the orbit. a) The cut-off power-law normalization at 1 keV, b) The intrinsic hydrogen column density. c) The soft excess blackbody luminosity, assuming a distance of 8 kpc . d) The Iron line flux, e) The iron line equivalent width calculated for the unabsorbed continuum, and f) the unabsorbed flux. Dashed vertical lines indicates the eclipse boundary.

Table 4. Spectral analysis results. All the free parameters are listed below together with unabsorbed 2-10 keV flux and χ^2_{ν} . All the uncertainties have been calculated at 90% confidence level. For more details see the text.

Phase (± 0.01)	N_H 10^{22} cm^{-2}	unabs EW (Fe) keV	Fe line flux $10^{-5} \text{ ph cm}^{-1} \text{ s}^{-1}$	Blackbody Luminosity $10^{33} \text{ ergs s}^{-1} @ 8 \text{ kpc}$	$\Gamma_v^{cutoffpl}$ (1 keV) $10^{-3} \text{ ph keV}^{-1} \text{ cm}^{-2} \text{ s}^{-1}$	F_{unabs} $2-10 \text{ keV}$ $10^{-10} \text{ erg s}^{-1} \text{ cm}^{-2}$	χ^2_{ν} (dof)
0.01	17^{+14}_{-9}	0.50 ± 0.4	0.34 ± 0.21	< 0.88	$0.015^{+0.009}_{-0.006}$	0.0054 ± 0.003	1.34 (23)
0.03	26^{+9}_{-6}	0.81 ± 0.4	$0.66^{+0.12}_{-0.15}$	< 0.33	$0.018^{+0.009}_{-0.005}$	$0.006(8) \pm 0.003$	2.6 (17)
0.08	18^{+10}_{-9}	1.1 ± 0.6	1.1 ± 0.3	< 0.57	$0.023^{+0.012}_{-0.007}$	$0.008(8) \pm 0.003$	1.06 (11)
0.15	15.7 ± 0.5	0.04 ± 0.01	$2.6^{+0.8}_{-0.6}$	1.6 ± 1.4	1.44 ± 0.03	0.48 ± 0.02	0.90 (172)
0.27	$9.4^{+0.4}_{-0.3}$	0.14 ± 0.02	14 ± 02	$4.4^{+0.3}_{-0.1}$	2.29 ± 0.05	0.77 ± 0.02	1.05 (128)
0.37	12.1 ± 0.3	0.09 ± 0.006	16^{+1}_{-2}	$3.4^{+0.2}_{-0.3}$	$3.86^{+0.05}_{-0.06}$	1.29 ± 0.04	1.09 (396)
0.40	19.1 ± 0.5	0.11 ± 0.01	11 ± 1	$2.81^{+0.06}_{-0.1}$	2.26 ± 0.05	0.76 ± 0.02	1.45 (207)
0.65	24 ± 1	0.11 ± 0.02	$7.6^{+0.9}_{-1.5}$	$1.87^{+0.1}_{-0.06}$	$1.55^{+0.06}_{-0.05}$	0.52 ± 0.02	0.99 (73)
0.79	23 ± 3	0.09 ± 0.03	$2.5^{+1.0}_{-0.7}$	< 1.48	0.60 ± 0.06	0.20 ± 0.04	0.97 (31)
0.91	89^{+11}_{-14}	0.12 ± 0.03	$3.2^{+0.5}_{-0.7}$	$1.41^{+0.1}_{-0.05}$	$0.6^{+0.2}_{-0.1}$	0.20 ± 0.07	0.82 (33)

of the neutron star. Hydrodynamical simulations (Blondin et al. 1990, 1991; Blondin 1994; Blondin & Woo 1995; Mauche et al. 2008) of HMXB have shown that the wind can be highly disrupted by the neutron star beyond the orbit.

To estimate the terminal velocity of the unperturbed wind, we have studied the N_H variability using three different sets of parameters (Fig. 5). The mass-loss rate and terminal velocity are constrained by the data to be in the range $\dot{M}_w/v_{\infty} \sim (0.7 - 2) \times 10^{-16} \text{ M}_{\odot}/\text{km}$; (β has a very limited impact on the results, we used 0.7).

The fraction of the wind captured by the neutron star can be estimated from the accretion radius $r_{acc} = 2GM_X/(v_{orb}^2 + v^2) \sim 2 \cdot 10^{11} \text{ cm}$ (where $v_{orb} = 250 \text{ km/s}$ is the orbital velocity) as $f \sim \pi r_{acc}^2/4\pi R_{orb}^2 \sim 7.5 \cdot 10^{-4}$. The mass-loss rate is therefore $\dot{M}_w \sim f^{-1} \dot{M} \approx 1.5 \cdot 10^{-6} \text{ M}_{\odot}/\text{yr}$ and the terminal velocity of the wind constrained in the interval $v_{\infty} \sim 250 - 600 \text{ km/h}$.

In our simulation we have adopted a terminal velocity $v_{\infty} = 400 \text{ km/sec}$, a stellar radius $R_* = 29 R_{\odot}$, a wind gradient $\beta = 0.7$, and a mass loss rate $\dot{M}_* = 1.35 \times 10^{-6} \text{ M}_{\odot} \text{ yr}^{-1}$. A summary of the assumed, observed, and inferred parameters of the model is listed in table 5. The variability of N_H along the orbit indicates that the unperturbed wind is adequate for phases $\phi \approx 0 - 0.35$. For $\phi \gtrsim 0.35$, N_H is increasing by $\sim 2 \times 10^{23} \text{ cm}^{-2}$. This indicates that a high density tail-like structure lies on one side of the orbit, trailing the neutron star. The tail-like component is still present up to $\phi \gtrsim 0.8$.

We have assumed that, the tail-like structure is created very close to the NS and is opening with distance from the neutron star. The density of the material inside the ‘tail’ is decreasing with distance for mass conservation. Its distribution follows a ‘horn’-like shape with a circular section. We have adjusted the density of the tail-like structure to match the observations. The density distribution $\rho_{wind} + \rho_{tail}$ is displayed in figure 6. The supergiant is located at the center (black disk). The tail-like structure covers about half of the orbit.

Figure 5 displays the simulated N_H variability from the above density distribution together with the observed data points. The data and the model shows that the tail-like perturbation is essential to understand the observed variations of the N_H .

Variability of the Fe $K\alpha$ line along the orbit

Assuming that the intrinsic X-ray flux is not affected by the eclipse, the Fe $K\alpha$ equivalent width drops by a factor ~ 10 during the eclipse in an orbital phase interval of ~ 0.1 . This indicates that the radius of the region emitting Fe $K\alpha$ is smaller than half

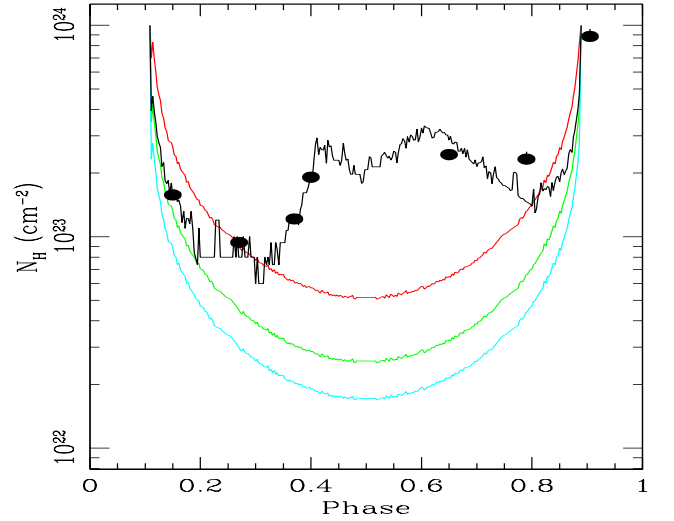


Fig. 5. Simulated N_H variations plotted together with the data. We illustrate three different wind configurations, for $\dot{M}/v_{\infty} = 0.7$ (cyan), 1 (green), and 2 (red) $\times 10^{-16} \text{ M}_{\odot}/\text{km}$, keeping all the other parameters fixed. The solid black line shows the total N_H consisting of the unperturbed stellar wind (green line) and of the tail-like extended component. The observations during the eclipse have been omitted.

of the stellar radius ($< 10^{12} \text{ cm}$) and much more compact than the tail structure responsible for the N_H variability profile.

Vela X-1 shows a similar behavior that was interpreted with an emitting region of the size of (Ohashi et al. 1984), or even within (Endo et al. 2002), the accretion radius.

Outside of the eclipse, the equivalent width of the Fe $K\alpha$ line is of the order of 100 eV. Following Matt (2002) and assuming a spherical transmission geometry, this corresponds to a column density of $N_H \sim 2 \cdot 10^{23} \text{ cm}^{-2}$. As this additional absorption is not observed, the region emitting Fe $K\alpha$ is partially ionized.

A ionization parameter $\xi = L/nR^2$ in the range 10–300 is required to fully ionize light elements contributing to the soft X-ray absorption and to keep an Fe $K\alpha$ line at the energy of 6.4 keV (Kallman et al. 2004; Kallman & McCray 1982). The density of the Fe $K\alpha$ emitting region is therefore $\sim \xi^{-1} R_{12}^{-2} \cdot 10^{12} \text{ cm}^{-3}$, where R_{12} is the distance from the neutron star in units of 10^{12} cm . As $N_H = nR \sim 2 \times 10^{23} \text{ cm}^{-2}$ we have $\xi \sim 5/R_{12}$. A dense cocoon is therefore needed around the neutron star with a size $0.5 > R_{12} > 0.02$ and a density $10^{11} \text{ cm}^{-3} < n < 3 \cdot 10^{12} \text{ cm}^{-3}$.

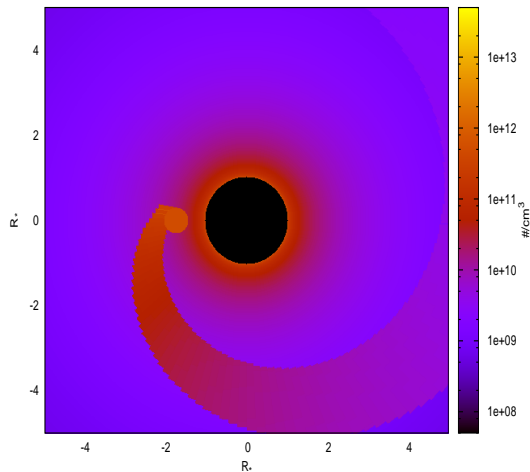


Fig. 6. Number density distribution in the plane of the orbit including a smooth wind and a tail-like perturbation. The black disk at the center represents the supergiant star.

To match the observed column density variability, the radius and the density of the inner region of the tail structure were set to $4 \cdot 10^{11}$ cm and $3 \cdot 10^{11}$ cm $^{-3}$ respectively. It is therefore very likely that the dense cocoon corresponds to the inner and ionized region of the hydrodynamical tail.

We have thus added this partially ionized cocoon in our simulations, using a density of $3 \cdot 10^{11}$ cm $^{-3}$ within a radius of $\sim 6 \cdot 10^{11}$ cm $\sim 3 R_{\text{acc}}$. The Fe K α emissivity map (Fig. 8) is built applying an illuminating radiation field ($\sim 1/r^2$) to the density distribution.

Figure 7 displays the resulting simulated profile of the Fe K α equivalent width together with the observed data. The green curve shows the variations of the Fe K α equivalent width expected from the wind density profile excluding the central cocoon, which obviously could not reproduce the data. The black curve accounts for the dense central cocoon. The exact profile of the eclipse is related to the size and density profile of the cocoon. No effort has been made to obtain an exact match to the data.

The ionized cocoon is expected to produce an iron K-edge at ~ 7.8 keV. For a column density of $N_{\text{H}} \sim 2 \times 10^{23}$ cm $^{-1}$, the optical depth of this edge $\tau \sim 0.2$ (Kallman et al. 2004) remains difficult to detect. Even our observation at an orbital phase 0.14 (the best candidate for the detection of the ionised edge) does not have enough signal.

The mass of the tail-like structure $M_{\text{tail}} \sim 10^{-8} M_{\odot}$ can be accumulated in $t_{\text{tail}} = M_{\text{tail}}/\dot{M}$, where $\dot{M} = (\pi r_{\text{eff}}^2/4\pi R_{\text{orb}}^2)\dot{M}_w$, where r_{eff} is an effective radius for the funneling of the wind in the tail. For a tail accumulation time scale (t_{tail}) comparable to the orbital period of (~ 10 days), this effective radius becomes $12 R_{\text{acc}}$.

The orientation of the tail-like structure depends on the wind and orbital velocity. The angle between the wind velocity and the orbital velocity is given by $\tan(\alpha) = v_{\text{orb}}/v$. The tail obtained in our simulations is tilted by $\alpha \sim 80^\circ$. This would correspond to $v \sim 0.2 v_{\text{orb}} \approx 50$ km/s which is lower than $v(R_{\text{orb}}) \approx 250$ km/s because of the ionization of the stellar wind in the vicinity of the neutron star.

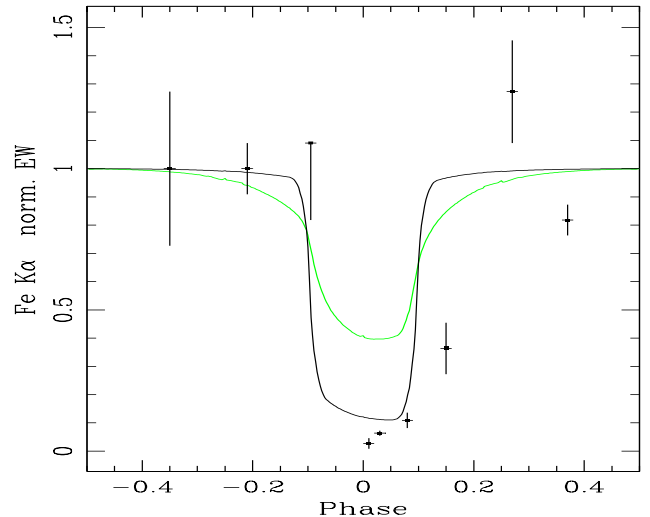


Fig. 7. Corrected unabsorbed Fe K α line equivalent width along the orbit. The two curves represent two different configurations in the presence of the hydrodynamical structure. *Black curve*: the central cocoon is present. *Green curve*: without the central cocoon. See the text for more details.

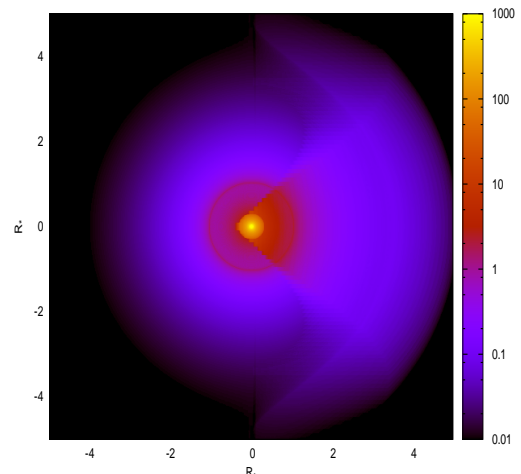


Fig. 8. Integrated Fe K α emissivity centered on the neutron star at phase $\phi = 0.5$ (relative units). The smooth circular halo shows the rim of the supergiant star. The tail structure can be observed on the right.

6. Conclusions

We have presented the analysis of an observing campaign performed with *XMM-Newton* on the persistently absorbed sgHMXB IGR J17252 – 3616. Nine observations have been performed over about four weeks, distributed on various orbital phases. Three of them were scheduled during the eclipse of the neutron star by the companion star.

We first refined the orbital solution, using in addition archival *INTEGRAL* and *RXTE* data and found an orbital period of 9.742 d and a projected orbital radius of 101 ± 2 lt-s. The pulsar spin period varies between 414.3 and 413.8 sec during the observing campaign.

The X-ray spectrum (0.2 – 10 keV), which varies along the orbit, was successfully fit using an absorbed cut-off power law

Table 5. Summary of the wind model used for IGR J17252 – 3616.

Parameter	Value	Reference
<i>Observed</i>		
$q=M_X/M_{OB}$	0.1	Mason et al. (2009b)
$M_{OB} (M_\odot)$	15	Takeuchi et al. (1990)
$\alpha (R_*)$	1.75	This work.
$\dot{M} (M_\odot/\text{yr})$	10^{-9}	This work.
<i>Assumed</i>		
$R_* (R_\odot)$	29	
$M_X (M_\odot)$	1.5	
i (deg)	90	
β	0.7	
<i>Inferred</i>		
v_∞ (km/s)	400	
$\dot{M}_w (M_\odot/\text{yr})$	1.35×10^{-6}	

continuum, a soft excess and a gaussian emission line. The soft excess, modeled with a black body, remained constant.

The continuum component varies in intensity (a measure of the instantaneous accretion rate) but features a constant spectral shape, as usually observed in accreting pulsars.

The absorbing column density and the Fe $K\alpha$ emission line show remarkable variations. The column density, always above 10^{23} cm^{-2} , increases towards 10^{24} close to the eclipse, as expected for a spherically symmetric wind. The wind velocity is unusually small with $v_\infty = 400 \text{ km/s}$. An additional excess of absorption of $2 \cdot 10^{23} \text{ cm}^{-2}$ is observed for orbital phases $\phi > 0.3$ revealing an hydrodynamical tail, trailing the neutron star.

During the eclipse, the equivalent width of the Fe $K\alpha$ line drops by a factor > 10 indicating that most of the line is emitted in a cocoon surrounding the pulsar, with a size of a few accretion radii. This cocoon is ionized and corresponds to the inner region of the hydrodynamical tail

The parameters of the IGR J17252 – 3616 are very similar to these of Vela X-1, excepting for the smaller wind velocity. We argue that the persistently large absorption column density is related to the hydrodynamical tail, strengthened by the low wind velocity. The tail is a persistent structure dissolving on a time scale comparable to the orbital period.

Our interpretation can be tested using numerical hydrodynamical simulation and high resolutions optical/infrared spectroscopy. If confirmed, it may turn out that half of the persistent sgHMXB have stellar wind speeds several times lower than usually measured.

Acknowledgements. This research has made use of NASA's Astrophysics Data System.

References

Arnaud, K. A. 1996, in *Astronomical Society of the Pacific Conference Series*, Vol. 101, *Astronomical Data Analysis Software and Systems V*, ed. G. H. Jacoby & J. Barnes, 17–+

Blondin, J. M. 1994, *ApJ*, 435, 756

Blondin, J. M., Kallman, T. R., Fryxell, B. A., & Taam, R. E. 1990, *ApJ*, 356, 591

Blondin, J. M., Stevens, I. R., & Kallman, T. R. 1991, *ApJ*, 371, 684

Blondin, J. M. & Woo, J. W. 1995, *ApJ*, 445, 889

Castor, J. I., Abbott, D. C., & Klein, R. I. 1975, *ApJ*, 195, 157

Charles, P. A. & Coe, M. J. 2006, *Optical, ultraviolet and infrared observations of X-ray binaries*, ed. Lewin, W. H. G. & van der Klis, M., 215–265

Chaty, S., Rahoui, F., Foellmi, C., et al. 2008, *A&A*, 484, 783

Corbet, R. H. D. 1986, *MNRAS*, 220, 1047

Courvoisier, T., Walter, R., Beckmann, V., et al. 2003, *A&A*, 411, L53

Dickey, J. M. & Lockman, F. J. 1990, *ARA&A*, 28, 215

Endo, T., Ishida, M., Masai, K., et al. 2002, *ApJ*, 574, 879

Fürst, F., Kreykenbohm, I., Pottschmidt, K., et al. 2010, *ArXiv e-prints*

Güdel, M. & Nazé, Y. 2009, *A&A Rev.*, 17, 309

Haberl, F. 1991, *A&A*, 252, 272

Hickox, R. C., Narayan, R., & Kallman, T. R. 2004, *ApJ*, 614, 881

Jansen, F., Lumb, D., Altieri, B., et al. 2001, *A&A*, 365, L1

Joss, P. C. & Rappaport, S. A. 1984, *ARA&A*, 22, 537

Kallman, T. R. & McCray, R. 1982, *ApJS*, 50, 263

Kallman, T. R., Palmeri, P., Bautista, M. A., Mendoza, C., & Krolik, J. H. 2004, *ApJS*, 155, 675

Lebrun, F., Leray, J. P., Lavocat, P., et al. 2003, *A&A*, 411, L141

Levine, A. M., Rappaport, S., Remillard, R., & Savcheva, A. 2004, *ApJ*, 617, 1284

Liu, Q. Z., van Paradijs, J., & van den Heuvel, E. P. J. 2006, *A&A*, 455, 1165

Mason, A. B., Clark, J. S., Norton, A. J., Negueruela, I., & Roche, P. 2009a, *A&A*, 505, 281

Mason, A. B., Norton, A. J., Clark, J. S., Negueruela, I., & Roche, P. 2009b, *ArXiv e-prints*

Matt, G. 2002, *MNRAS*, 337, 147

Mauche, C. W., Liedahl, D. A., Akiyama, S., & Plewa, T. 2008, in *American Institute of Physics Conference Series*, Vol. 1054, *American Institute of Physics Conference Series*, ed. M. Axelsson, 3–11

Ohashi, T., Inoue, H., Koyama, K., et al. 1984, *PASJ*, 36, 699

Press, W. H. & Rybicki, G. B. 1989, *Astrophysical Journal*, 338, 277

Quaintrell, H., Norton, A. J., Ash, T. D. C., et al. 2003, *A&A*, 401, 313

Rahoui, F., Chaty, S., Lagage, P., & Pantin, E. 2008, *A&A*, 484, 801

Schulz, N. S., Canizares, C. R., Lee, J. C., & Sako, M. 2002, *ApJ*, 564, L21

Strüder, L., Briel, U., Dennerl, K., et al. 2001, *A&A*, 365, L18

Takeuchi, Y., Koyama, K., & Warwick, R. S. 1990, *PASJ*, 42, 287

Tawara, Y., Yamauchi, S., Awaki, H., et al. 1989, *Astronomical Society of Japan*, 41, 473

Thompson, T. W. J., Tomsick, J. A., in 't Zand, J. J. M., Rothschild, R. E., & Walter, R. 2007, *ApJ*, 661, 447

van Kerkwijk, M. H., van Paradijs, J., Zuiderwijk, E. J., et al. 1995, *A&A*, 303, 483

Walter, R. 2010, in press

Walter, R., Bodaghee, A., Barlow, E. J., et al. 2004, *The Astronomer's Telegram*, 229, 1

Walter, R., Zurita Heras, J., Bassani, L., et al. 2006, *A&A*, 453, 133

Warwick, R. S., Norton, A. J., Turner, M. J. L., Watson, M. G., & Willingale, R. 1988, *MNRAS*, 232, 551

Watanabe, S., Sako, M., Ishida, M., et al. 2006, *ApJ*, 651, 421

Winkler, C., Courvoisier, T., Di Cocco, G., et al. 2003, *A&A*, 411, L1

Zurita Heras, J. A., de Cesare, G., Walter, R., et al. 2006, *A&A*, 448, 261